Smart Materials and Structures

Enabling tunable micromechanical bandpass filters through phase-change materials

IOP Publishing Smart Materials and Structures
Smart Mater. Struct. **26** (2017) 085032 (12pp) https://doi.org/10.1088/1361-665X/aa7545

Enabling tunable micromechanical bandpass filters through phase-change materials

Yunqi Cao, David Torres, Tongyu Wang, Xiaobo Tan and Nelson Sepúlveda[1]

Department of Electrical and Computer Engineering, Michigan State University, East Lansing, MI 48824, United States of America

E-mail: caoyunqi@msu.edu, torresd5@egr.msu.edu, wangton3@msu.edu, xbtan@egr.msu.edu and nelsons@egr.msu.edu

Received 15 March 2017, revised 17 May 2017
Accepted for publication 26 May 2017
Published 19 July 2017

Abstract

Vanadium dioxide (VO_2), one of the most promising phase-change smart materials, has shown strong frequency tuning capabilities in MEMS resonators. In this paper, we demonstrate the potential use of VO_2-based MEMS devices as second-order kilohertz (kHz) bandpass filters with tunable band selectivity and adjustable bandwidth (BW). Two identical on-chip micro resonators are actuated using mechanical excitation and measured using optical detection. One of the resonators is not actuated while the other is tuned by applying electric currents across an integrated resistive heater, which induces the phase transition of the VO_2, and consequently a large stress to the mechanical structure. The responses of both MEMS resonators are combined, resulting in a resonant peak of tunable BW controlled by the input current. The BW can be extended to 2.62 times by using two bridges or 2.39 times by implementing one pair of cantilevers. The results for both devices are discussed.

Supplementary material for this article is available online

Keywords: vanadium dioxide, phase-change, MEMS, bandpass filter

(Some figures may appear in colour only in the online journal)

1. Introduction

In modern signal processing and transceiver technologies, electromechanical resonators have been widely implemented in RF circuits (e.g. oscillators, mixers, and filters) and sensing (e.g. temperature, mass, and humidity) applications. Their small size is a key advantage, which enables scaling for transceiver miniaturization and sensitivities as high as 7×10^{-21} g and 13.89 pm K^{-1} for mass and temperature sensors, respectively [1, 2].

The applications of MEMS resonators have expanded as the technology has matured. Progress in micro-fabrication processes, design, and materials synthesis has made possible the cost-effective integration of micro-electro-mechanical resonators into electronic circuits [3]. In fact, MEMS resonator technologies are commonly preferred over their predecessor technologies that were based on the quartz crystal-based oscillators. Main advantages of MEMS include: (i) small size, (ii) feasibility for on-chip integration of IC active or processing circuitry, (iii) accurate timing synchronization with external devices, and (iv) low power consumption.

MEMS resonators can provide resonant frequencies that extend to ultra high frequency (UHF) range with Q-factors as high as 2.2×10^5 [4]. The high selectivity that comes with narrowband high-Q MEMS resonators is ideal for some applications that require low noise and larger number of communication channels. For broadband circuits in RF circuits, such as band-pass filters, coupled resonators have been used to demonstrate high order MEMS band-pass filters. Coupling techniques can be mechanical or electrical.

[1] Author to whom any correspondence should be addressed.

Mechanical coupling requires rather complicated fabrication and precise design for generating multiple pole systems [5–7]. Using electrical coupling methods usually involves capacitive coupling or cascading of multiple resonators [8]. The merit of using electrical coupling lies in the flexibility of design, the ability of extending the resonant frequency into UHF range, and a more precise bandwidth (BW) tunability. However, electrical coupling also adds extra complexity to the system.

Most of the advances in MEMS have been made along the lines of using silicon and other common CMOS standard and compatible materials. This trend for technological improvement has been exploited through the use of strategic and complicated geometries, which provides excellent performance for well-defined applications. However, the improvement achieved by using complex structures is ultimately limited by the underlying physical capabilities of the materials used. This is why many recent efforts have been focused on the characterization and integration of non-standard materials in MEMS [9–12]. For example, VO_2 was recently introduced as a smart material in MEMS, demonstrating the highest energy densities [13, 14], programmable mechanical states [15], MEMS mirrors [16], and electro-optical states [17]. In this work, we are now using VO_2 to demonstrate the potential use of its phases transition in MEMS tunable filters.

VO_2 is a phase-change smart multifunctional material with a fast insulator-to-metal transition (IMT) induced upon heating, during which the crystal structure changes from its low temperature monoclinic phase to its high temperature rutile phase. The phase transition typically begins at ~68 °C and spans ~10 °C–15 °C. The material's electrical [18], optical [19], and mechanical [13] properties change drastically during the IMT and show hysteretic behavior. When VO_2 is used as a thin film coating over a micro-mechanical structure, the changes in the mechanical properties generate large stress [13, 20] that has been exploited to demonstrate high-performance MEMS actuators [21] with programmable capability [15]. These large stress levels could also be used to shift the resonant frequency of a micro-mechanical structure [22]. For a cantilever structure, the generated stress would be mostly released and transformed to bending. On the other hand, bridge structures do not have a free-end, and the generated stress is contained within the structure (unless the stress surpasses the Euler buckling limit).

In this paper, we demonstrate the potential use of VO_2 for the development of tunable MEMS bandpass filters. Two identical bridge or cantilever resonators, with similar resonant frequencies are used. The two resonators are driven by the same sweeping electrical AC source signal and the resonant frequencies for both resonators are optically detected simultaneously. In this design, the two resonators can independently respond to the same input at their own eigenfrequencies while producing one signal output. The BW tuning is achieved by actuating one of the resonators using joule heating. The Q-factor enhancement and the BW tunabilities for both structures are compared and analyzed at the end. The main contribution of this work is the demonstration of a new mechanism that can be implemented in MEMS tunable filters, which is based on the solid–solid phase transition of VO_2. The results demonstrate that, in very simple and non-optimized devices, the mechanism produces relatively large simultaneous tunability of BW and center frequency (f_o).

2. Experimental procedures

2.1. Design and fabrication of VO_2-based resonators

The VO_2-based resonator structures (cantilevers and bridges) reported in this paper are all within the same chip. Both resonator designs (i.e., cantilevers and bridges) share the same fabrication process flow, which has been described previously and is shown in figure 1 [23, 24]. Uncoated MEMS resonators (before VO_2 deposition) used in this paper are 2 μm thick, with a 200 nm layer of titanium/platinum (50 nm Ti / 150 nm Pt) heater electrode placed in between two 1 μm SiO_2 layers. This symmetric stack of layers was designed to reduce the extrinsic thermal stress during the deposition of the VO_2 thin film, which could produce bending of the structure in the process and an uneven VO_2 thin film deposition. In summary, an SiO_2 layer was deposited on a Si wafer using low thermal oxidation (LTO) method, followed by deposition and patterning of Ti/Pt (Ti only used for adhesion purposes), deposition of a second 1 μm layer of SiO_2 (again, using LTO), and patterning of the resonator structures through both SiO_2 layers. The wafers were then diced, and released, which was done by isotropic etching of the silicon substrate using xenon difluoride (XeF_2) gas. VO_2 thin film was deposited using pulsed laser deposition (PLD). During the deposition process, the chamber was first pumped down to a vacuum level below 10^{-6} Torr by using a turbomolecular pump connected with a mechanical scroll pump. Then the oxygen was introduced into the chamber at a flow rate of 20 sccm and a butterfly valve was controlled to keep the chamber oxygen atmosphere pressure at 15 mTorr. A heater located approximately 2 inches behind the sample was preheated to 595 °C. After reaching this temperature, a metallic vanadium target was ablated by a krypton fluoride (KrF) excimer laser with 560 mJ in energy and 10 Hz in frequency for 10 min. After VO_2 deposition, a 30 min annealing step was performed under the same deposition conditions. After the deposition was completed, a resistance measurement was done as the temperature was varied across the phase transition of VO_2. The measured drop in resistance of approximately 3 orders and the hysteretic behavior observed verified the quality of the VO_2 thin film.

At this point, the devices were ready to be mounted on an IC package, wire-bonded and tested. The fabricated and tested resonators, shown in figure 1, include two micro cantilevers (550 μm long and 50 μm wide) and two micro bridges (300 μm long and 45 μm wide).

For the VO_2 coated micro-bridges, the initial first mode resonant frequency can be estimated by the following

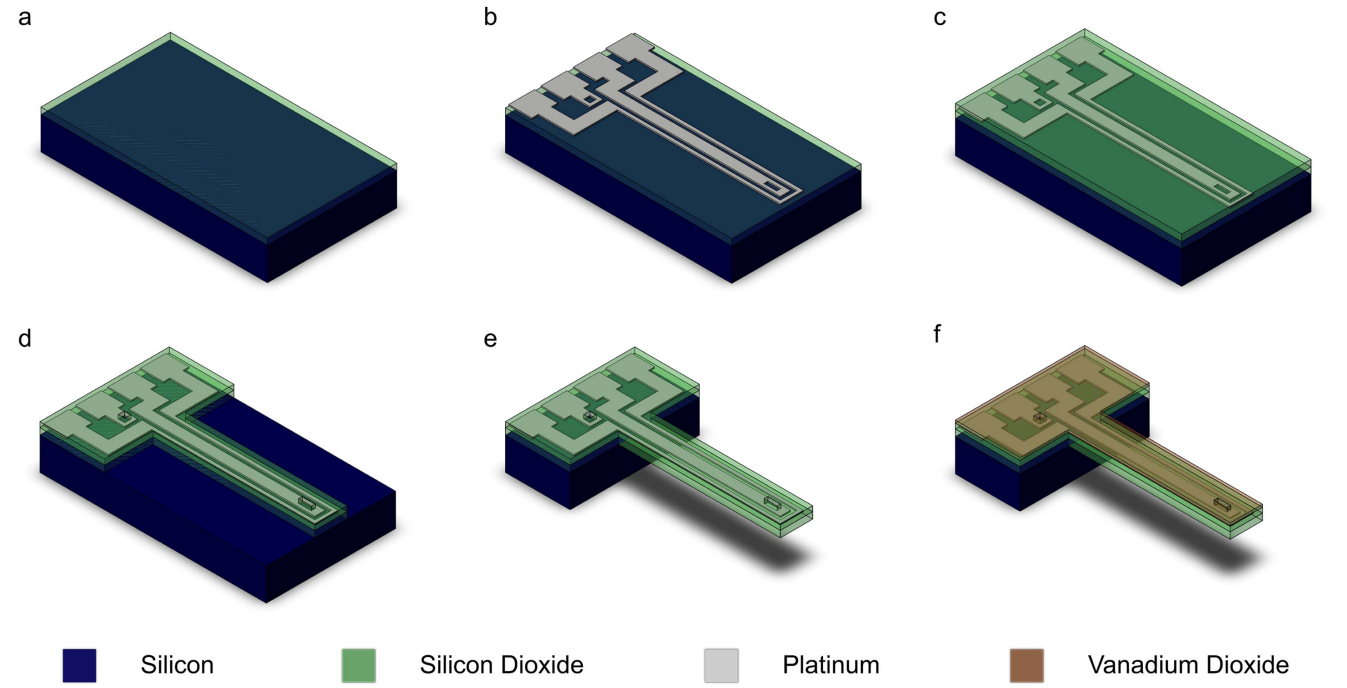

Figure 1. Fabrication flow of VO_2-based cantilever. (a) LTO deposition of SiO_2 layer on Si substrate, (b) thermal evaporation of Ti/Pt heater trace, patterned by lift-off, (c) LTO deposition of second layer SiO_2, (d) structure defined by dry etching, (e) MEMS structure released by XeF_2, (f) PLD deposition of VO_2 coating.

equation [25]:

$$f_b^2 = 1.06 \times \frac{[E_1^2 h_1^4 + E_2^2 h_2^4 + E_1 E_2 h_1 h_2 (4h_1^2 + 4h_2^2 + 6h_1 h_2)]}{(\rho_1 h_1 + \rho_2 h_2)(E_1 h_1 + E_2 h_2) l^4}, \quad (1)$$

where E_1, h_1, ρ_1 and E_2, h_2, ρ_2 are the Young's modulus, thickness and density of the SiO_2 and the VO_2 layer, respectively, and l is the length of the bridge. On the other hand, the initial first mode resonant frequency of the VO_2 coated cantilever can be given by [26]:

$$f_c^2 = \frac{0.26 h_1^2}{\pi^2 l^4} \times \frac{E_1 w h_1 + 12 E_2 h_2 \left[(w + 2h_2) \left(\frac{1}{2} + \frac{h_2}{h_1} + \frac{h_2^2}{2h_1^2} \right) + \frac{h_1}{6} \right]}{\rho_1 h_1 w + 2\rho_2 h_2 (w + h_1 + 2h_2)} \quad (2)$$

with the same variables used for equation (1) and w is the width of the cantilever. The equations above determine the initial resonant frequencies of the two resonator structures used in this work in the static state (i.e. un-actuated at room temperature). It should be noted that the equations do not take into account the thin metal layer used for Joule heating and tuning; but they do provide a good approximation that can be used for initial device design. As it is explained in more detail in section 3, the demonstration of the potential VO_2 based bandpass filter consisted of two identical resonators, where the resonant frequency of the static resonator remained constant, while the resonant frequency of the active resonator shifted according to the hysteresis curve (figure 3 left and figure 6 left) as the current increased. Thus, f_o of the bandpass filter can be estimated using equations (1) and (2). The calculated resonant frequencies are shown in figures 4 and 7 along with the experimental value. Here, a 9% under-etching effect [25] was assessed for the bridges and 4.5% for the cantilevers. Thus, the effective length of the bridges and cantilevers were estimated to be 328 μm and 576 μm respectively. The resonant frequency of the bridges determined by equation (1) is about 102.3 kHz, which is far from the measured frequency shown in figure 4-right. This is due to the strong influence of stress in the resonant frequency of a bridge structure. To match the experimental curve, the initial residual stress in the bridge was estimated to be 38.9 MPa—which is within the value found for similar structures [25]. Thus, considering the stress effect, the resonant frequency for the bridge is found to be 237.6 kHz. It should be noted that this thermal residual stress does not play such a strong influence on the resonant frequnecy of cantilever structures, since the stress is partially released, producing an intial bending. Thus, the estimated resonant frequency of the cantilevers determined by equation (2) is 5.49 kHz, which is not that far from the measured resonant frequency shown in figure 7-right.

2.2. Experimental setup

The measurement setup used in this work is shown in figure 2. An LED white light source and a CCD camera were placed in the setup to help locate the devices on the chip. In this experiment, the resonant frequencies of both of static sample and the active sample were measured optically by monitoring the deflection of a laser beam incident on the mechanical structure. The laser source used here was a

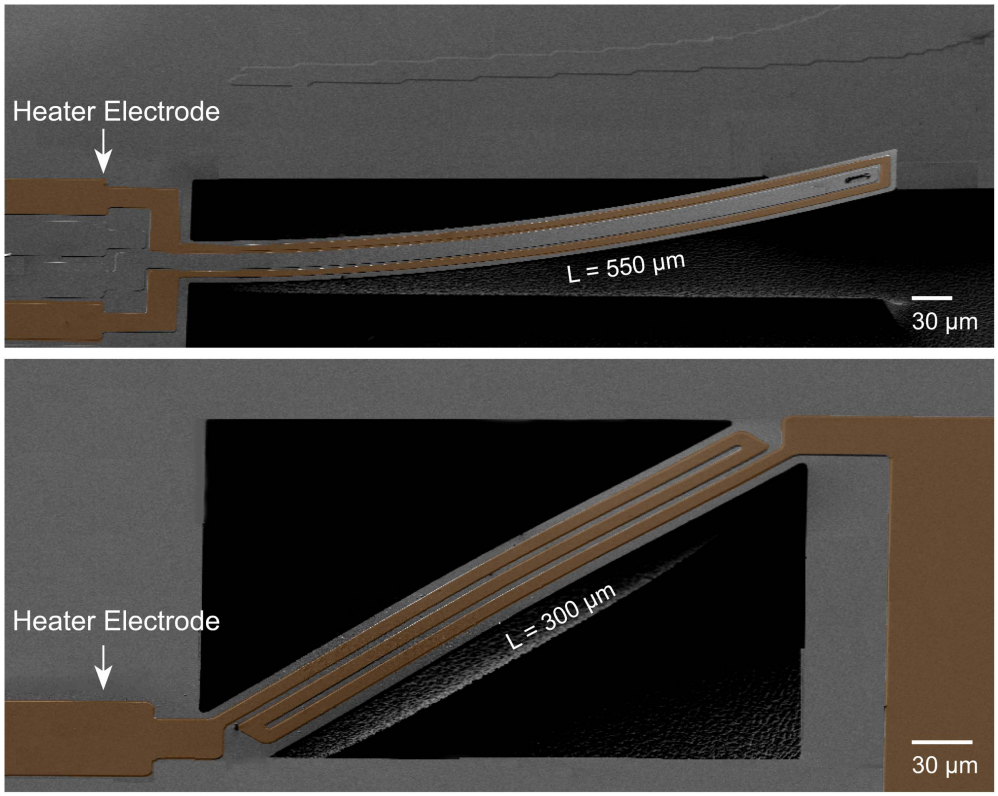

Figure 2. SEM images for the tested structures. Top: cantilever. Bottom: bridge. The electrodes for resistive heating actuation are artificially colored for clarity.

632.8 nm, 5 mW He–Ne laser. Light from the laser was redirected by a silver-coated reflective mirror and beam splitters in the optical path. Since the VO_2 thin film coating is thermally actuated and highly sensitive to temperature (especially in the transition region), light absorption from the laser could increase the film's temperature. To reduce this unwanted self-heating effect, a neutral density filter (ND = 1.0) was placed into the optical path to lower the power of the measuring laser beam to the minimum power that still provided enough detecting signal [27, 28].

After the first mirror and beam splitter, the beam was split and focused on both samples using two long working distance objectives (10X Mitutoyo MY10X-803 Objective lens). Each sample represented a chip that contained resonator structures that were fabricated simultaneously. A piezoelectric transducer was attached to the back of each sample, and both transducers were driven into mechancial vibration by the output signal of a network analyzer (HP3589A). The laser was focused on identical resonator structures, and the reflected beam was directed to a photodetector through another beam splitter. The output of the photodetector was connected to the input of the network analyzer. In this configuration, the network analyzer would display the voltage output of the photodetector as a function of frequency. The network analyzer drove the piezoelectric transducers at different frequencies, inducing the resonator's largest vibration amplitude at a frequency close to their natural frequency. Vibrations from the resonator structure produced oscillations in the reflected laser beam (of magnitude proportional to the vibration amplitudes), which were converted to a voltage by the photodetector and sent back to the network analyzer. It should be noticed that in this measurement setup, the input/output characteristics of the system does not require coupling of electrical and mechanical signals. The input signal applied to the filter system was a time-dependent electrical signal, but the actuation signal was the mechanical vibration provided by the piezoelectric transducer. The tuning signal is the current applied to the heater of the active element, which is an electrical signal, but the output is a mechanical vibration detected optically. This method is an adaptation of laser deflection and interferometer techniques commonly used to characterize MEMS—in fact, it also allows for the testing of a single resonator structure by simply blocking the optical path to one of the structures.

In the reported experiments, the temperature for one of the samples (active sample) was increased by applying a current to the integrated resistive heater (i.e. by Joule heating); while the other sample (static sample) remained at room temperature. The current supplied to the active sample was computer-controlled and provided through wire bonding connections to pads at the border of the chip. Both samples were mounted on two individual three-axis moving stages to facilitate alignment of the laser beam on the resonator structure.

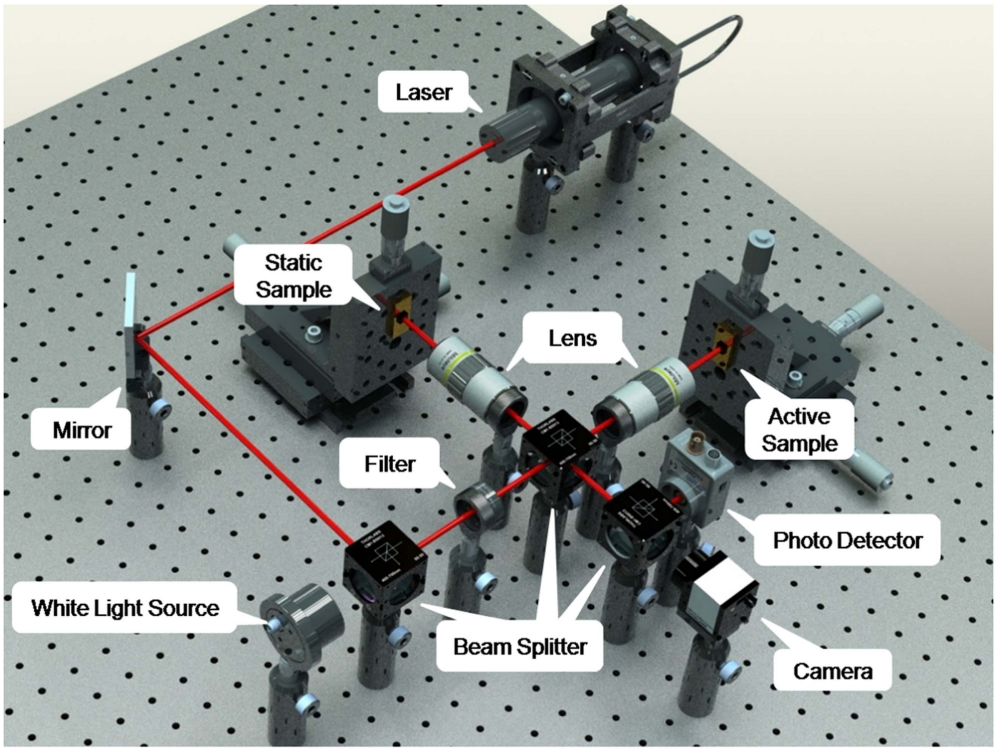

Figure 3. Experimental setup. The active sample is the resonator (cantilever or bridge) actuated by joule heating, while the static sample is the resonator (cantilever or bridge) that is not actuated. Two identical piezo-disks were placed underneath the static sample and the active sample respectively and they are sharing one driving AC source signal provided by the network analyzer. The output of the photo detector is connected to the input of the network analyzer. The laser beams passing through the beam splitters are not contributing to the measurement, and therefore are not shown for clarity.

3. Results and discussion

Two different structures of micro beam resonators (cantilevers and bridges) were tested in this experiment and the BW tunability of each structure was demonstrated and compared. The maximum BW amplification, Q-factor, and BW tuning window will be discussed in the following sections. The BW was calculated using the 3 dB of the resonant peak method using the following equation:

$$\mathrm{BW} = f_2 - f_1, \tag{3}$$

where BW stands for the bandwidth. f_1 and f_2 are the two frequencies on each side of the resonant frequency (f_r) where the amplitude of the signal is $1/\sqrt{2}$ of its maximum value. The Q-factor (Q) is then calculated based on the BW value using the equation as below [29]:

$$Q = f_r/\mathrm{BW}. \tag{4}$$

3.1. BW tunability for bridges

First, two identical bridges were used to create the bandpass filter. The active bridge was activated by Joule heating, and the resonant frequency was measured through the whole heating and cooling cycle (figure 3-left) by blocking the laser beam coming from the static sample. The frequency shift comes as the result of the large amount of stress generated by the VO_2 thin film coating during its phase transition region. When the laser beam coming from the static sample was unblocked, we were able to get two resonant signals, one from the static bridge and the other from the active bridge. These optical signals were routed to the photodetector, and its output to the network analyzer, which showed the resonant peaks for both devices. The top-left plot in figure 4 (Stage 'a') shows the output of the spectrum analyzer for both bridges at room temperature i.e. while the active bridge was not actuated ($I_{act} = 0$ mA). The current step is 0.01 mA within the BW tuning window and 0.1 mA for the outside region. It should be noted that, although both bridges are geometrically identical, their resonant frequencies at room temperature are not the same. This could be due to any slight difference between the fabrication processes of both devices; we believe that the most likely cause was a difference in 'effective length' [25, 30, 31] for the two structures, which could have occurred during isotropic release step.

When a current was applied to the active bridge (I_{act}), its resonant frequency would shift to a certain value according to the hysteresis curve shown in figure 3. Figure 4 shows a sequence of over-imposed resonant frequency peaks for the static and active bridges for different I_{act} values. The sequence starts at room temperature (Stage 'a'), goes through a heating cycle (increasing I_{act}), until the transition of VO_2 is completed (Stage e in figure 4). At this point, the cooling cycle begins (reducing I_{act}), until we reach room temperature again (Stage 'j' in figure 4). Starting at room temperature, the combination of both resonant peaks resembles the behavior of a band-pass

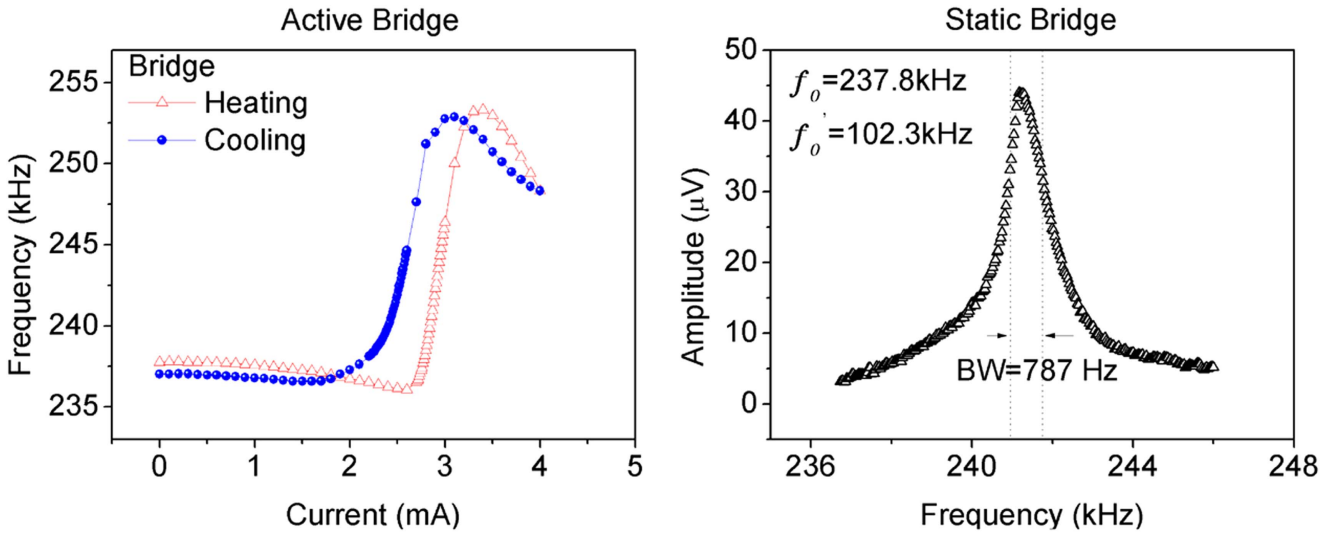

Figure 4. Left: resonant frequency versus actuation current through a full heating and cooling cycle for the active bridge. Right: resonant frequency signal for the static bridge at room temperature. The measured (f_0) and calculated (f_0') resonant frequencies are shown. The value for f_0' was obtained from equation (1), and it does not take residual thermal stress into account.

Table 1. Bandwidth tunability for bridges.

			Static bridge		
Bandwidth (Hz)			787		
Q-factor			306		
			Active heating		
Stage	A	B	C	D	E
Bandwidth (Hz)	Snap	732	1391	1849	Snap
Q-factor	NA	330	174	131	NA
I_{act} (mA)	0.00	2.89	2.91	2.92	3.00
			Active cooling		
Stage	F	G	H	I	J
Bandwidth (Hz)	Snap	2062	1607	666	Snap
Q-factor	NA	117	151	362	NA
I_{act} (mA)	2.70	2.57	2.55	2.52	0.00

filter; and its width is tuned by current steps of increasing magnitude that induce the phase transition of VO_2. As the actuation current increases from room temperature, the active peak moves towards the static peak, reducing the filter's BW. When $I_{act} = 2.89$ mA (b Stage), the active and static peaks show very similar resonant frequencies, and both responses are merged into one signal peak. Details on the combination of both resonant peaks is provided in the supplementary materials available online at stacks.iop.org/SMS/26/085032/mmedia. As I_{act} is further increased, the resonant frequency of the active bridge keeps increasing, and the active peak continues starts moving to the right of the static peak. At $I_{act} = 2.92$ mA (Stage 'd'), the resonant frequency of the active bridge begins to separate, and by $I_{act} = 3.00$ mA, the two f_r curves clearly become two separate peaks. The largest measured BW during the heating cycle was around 1.85 kHz (at $I_{act} = 2.92$ mA). The cooling cycle (Stage 'f' through 'j') was performed to demonstrate the reversibility of the system. As the actuation current decreases, the active peak moves towards the static peak and the peaks begin to merge at $I_{act} \sim 2.57$ mA. The maximum BW of the cooling cycle is around 2.06 kHz (at $I_{act} = 2.57$ mA), which is 2.62 times larger than a single device. As the current further decreases, the difference in the resonant frequencies become smaller. At $I_{act} = 2.52$ mA (Stage 'i') the two peaks become one; and the system goes back to its initial condition when I_{act} is turned off. The stages included in figure 4 are displayed for similar frequency measurements between the heating and cooling cycle i.e. the two plots in a single row show similar output. However, the I_{act} values are different between these similar stages. This is due to the hysteresis of VO_2 which does not show a linear correspondence between the two cycles (see figure 3).

It can be noticed that at the stages where the signal snaps into two individual peaks (Stages 'a', 'e', 'f', 'j'), the signal level for each individual peak is of equal amplitude to the signal of a single bridge (figure 3-right). However, for the stages which have extended BW (Stages 'b', 'c', 'd', 'g', 'h', 'i'), the signal level is higher than the one generated by the single bridge resonator. This is due to the additive effect of the two individual signals generated by the static resonator and the active resonator, which occurs only during stages with band-pass filter behavior. Also, at Stages 'b' and 'i', the BWs are smaller and therefore, a higher *Q*-factor is achieved (see table 1).

The resonant peak of the single static bridge used in this system has a BW of 787 Hz (see figure 3). Thus, a tunable BW amplification up to 2.62 was achieved by using one pair of identical bridges. It should be noted that, in this particular case, the shift in f_r for the active bridge 'crossed' the f_r of the static bridge. Therefore, the tunable BW could include different range of frequencies by increasing or reducing the separation between the two peaks at room temperature. It is

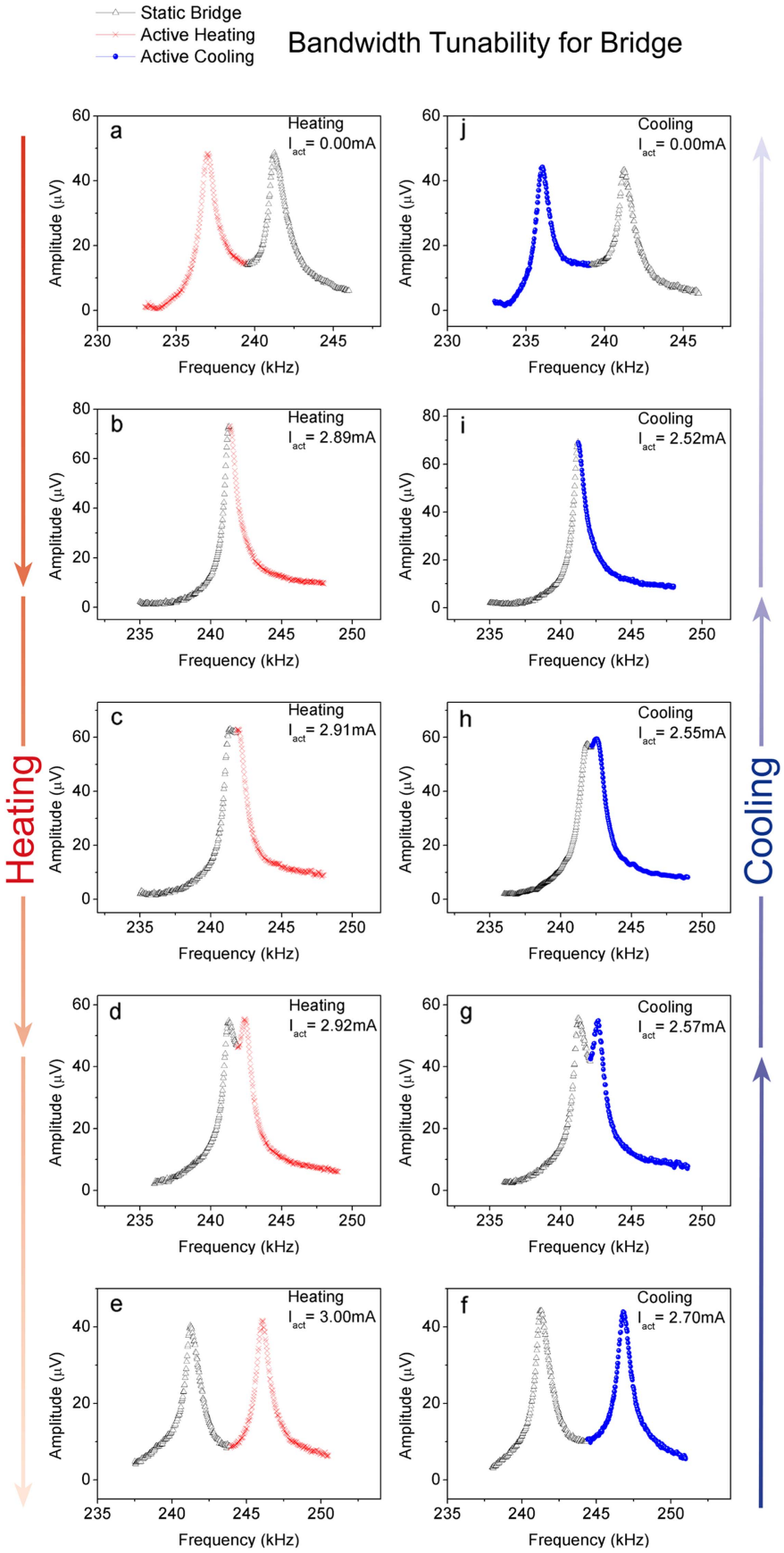

Figure 5. Sequence of different stages for the VO_2-based tunable band-pass filter using bridge resonators during a heating/cooling cycle. Plots show selected stages with pairs of similar output for each cycle. The resonant peaks for the static and active bridges are represented by the black and red/blue curves, respectively. I_{act} is the actuation current applied to the active bridge.

Table 2. Bandwidth tunability for cantilevers.

	Static cantilever				
Bandwidth (Hz)	135				
Q-factor	38				
	Active heating				
Stage	A	B	C	D	E
Bandwidth (Hz)	155	212	279	332	Snap
Q-factor	33	24	18	16	NA
I_{act} (mA)	3.0	3.4	4.2	5.4	6.2
	Active cooling				
Stage	F	G	H	I	J
Bandwidth (Hz)	Snap	331	284	228	174
Q-factor	NA	16	18	22	29
I_{act} (mA)	6.0	5.2	4.0	3.2	2.8

important to clarify that the applied current I_{act} is the tuning parameter, and not the input to the system that generates oscillation. During the entire heating-cooling cycle, the input is the frequency of the AC signal applied to the piezo-disks (supplied by the network analyzer). The measured output is the combined resonant peaks. The data for actuation current, BW and *Q*-factor is summarized in table 1.

3.2. BW tunability for cantilevers

The VO_2-based bandpass filter could also be achieved by using a pair of identical cantilever structures. The measurement method and the tuning method are the same as those used for bridges. The BW tunability is shown in figure 5 and all the related data is summarized in table 2. The resonant frequency of the active peak follows the hysteresis curve shown in figure 6-left. The resonant frequency signal for the single static cantilever was measured (figure 6-right) and the BW was calculated to be 135 Hz. The starting stage here is chosen to be the one with an $I_{act} = 3.0$ mA rather than 0 mA. The reason is that the initial bending of this active cantilever cannot produce a signal comparable to that of the static cantilever. Nevertheless, this difference does not affect significantly the results obtained and drawn conclusions, since the difference between the resonant frequency at $I_{act} = 0.0$ mA and at 3.0 mA was found to be only 12 Hz. The maximum BW for this system is reached at $I_{act} = 5.4$ mA and at $I_{act} = 5.2$ mA for the heating and cooling cycles, respectively. The maximum BW obtained by this system is about 322 Hz, which is 2.39 times the BW of a single cantilever.

3.3. BW tunability comparison

The room temperature measurement in figure 5 (Stage 'a') shows that the f_r for both cantilevers (active and static) are much closer than the f_r for both bridges at room temperature. When both devices were measured independently, the difference in f_r between the active and static devices was found to be about 8% and 1% for the bridges and cantilevers, respectively. This supports the claim that different effective lengths due to irregular under-etching during isotropic release play a major role in the different f_r for the two bridges at room temperature. A bridge structure has two anchors, and therefore, a difference in the effective length due to under-etching difference will have a stronger influence in a bridge structure than in a cantilever structure. Due to the much smaller difference in the f_r for the cantilevers, the measurement at room temperature for both cantilevers (active and static) is simply a slightly broader peak than the single cantilever, shown in figure 6. Unlike the case for the bridges, as the tuning actuation begins for the active cantilever (by increasing I_{act}), the BW begins to increase monotonically during the heating cycle. There is no 'crossing' between resonant peaks for the cantilevers. This monotonic BW tuning behavior for the cantilever also holds during the cooling cycle. Another striking difference between both results is the required 'tuning energy'. Starting at the on-set of the phase transition, crossing the entire phase-change to generate maximum deflection in cantilevers requires $I_{act} \sim 3.5$ mA (figure 6-left), while the bridges require less than 0.75 mA (figure 3-left).

The actuation current required to reach the maximum BW for the cantilevers and the bridges (from stage A to stage D for the cantilevers and from stage b to stage d for the bridges) is 2.4 and 0.03 mA, respectively. Considering the resistance of the heater traces of the cantilevers and bridges (285 and 245 Ω, respectively), the power consumption for maximum BW tuning is calculated to be 5.75 mW for the cantilever, and 0.04 mW for the bridge structures.

The main reason for this larger energy requirement for the cantilever relates to two main differences between the device structures: (i) thermal mass, and (ii) heat distribution. Notice that the bridge structures are almost half as long as the cantilever structures. A larger length translates to a larger thermal mass, which means that a larger amount of energy will be required to increase temperature. Thus, it is more energy demanding to induce the phase transition of VO_2 in the cantilever structure than in the bridge structure. Also, note that the heater design for the bridge covers a larger surface of the bridge structure, which allows for a more uniform. Finally, there is a significant difference between the change in frequency for the active device per unit current (i.e., sensitivity); and the total tuning range between bridges and cantilevers. The explanation for the different sensitivities and tuning ranges share the thermal mass issue described above—a larger energy is required in a cantilever structure to induce the same temperature increase; but this mechanism does not play a major role. The dominant mechanism (for both larger sensitivity and tuning range) relates to the stronger dependence of resonant frequency with stress for the bridge structure. In fact, this higher sensitivity of the resonant frequency of a bridge structure to stress is the reason why the pairs of equivalent stages in the heating and cooling cycle look more similar for the cantilevers than for the bridges. The tuning experiments for the cantilevers involved current steps of 0.1 mA, while the bridges required steps 10 times smaller.

The relation between the resonant frequency and the stress for both structures is now qualitatively discussed.

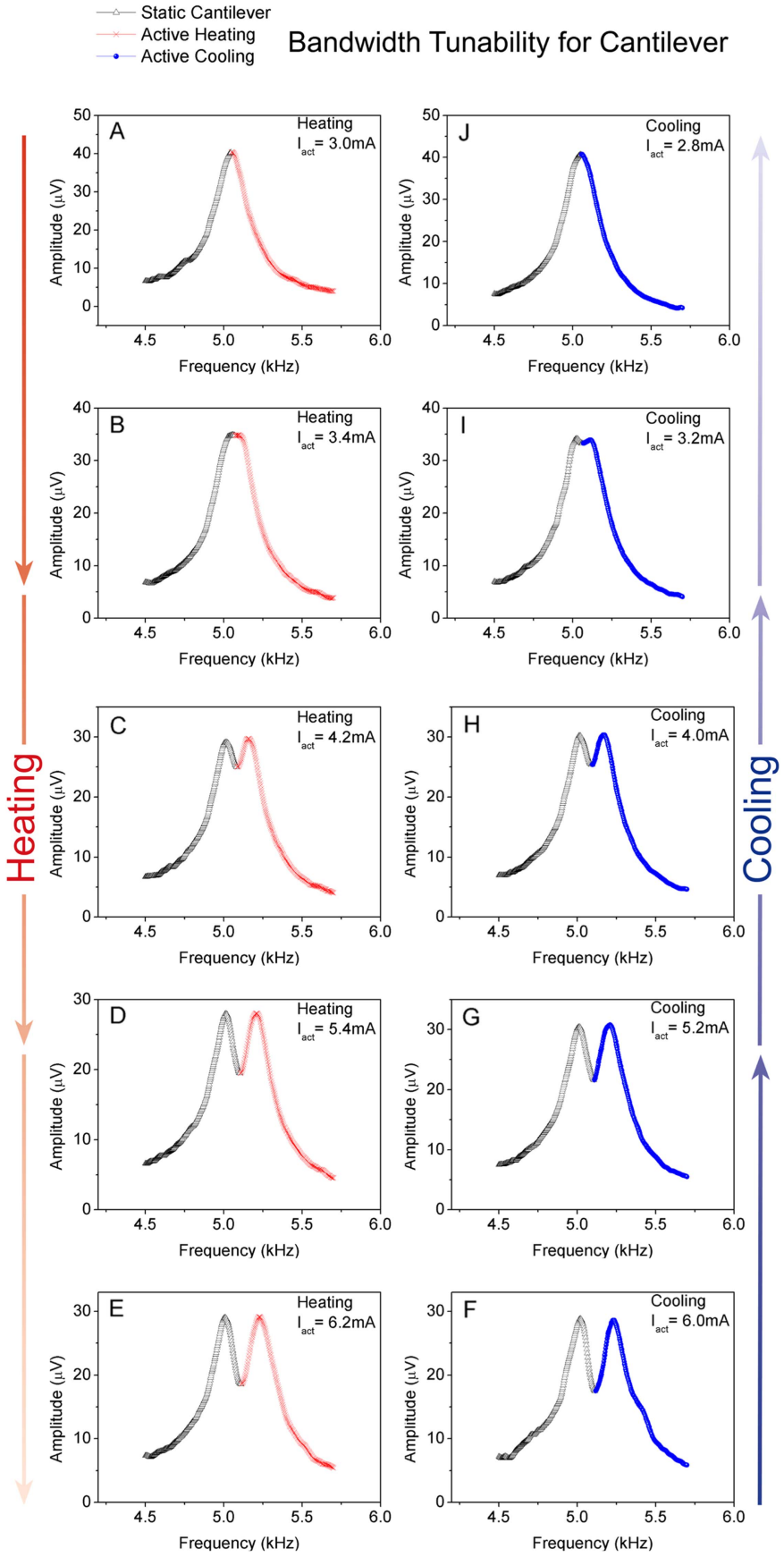

Figure 6. Sequence of different stages for the VO_2-based tunable band-pass filter using cantilever resonators during a heating/cooling cycle. Plots show selected stages with pairs of similar output for each cycle. The resonant peaks for the static and active bridges are represented by the black and red/blue curves, respectively. I_{act} is the actuation current applied to the active bridge.

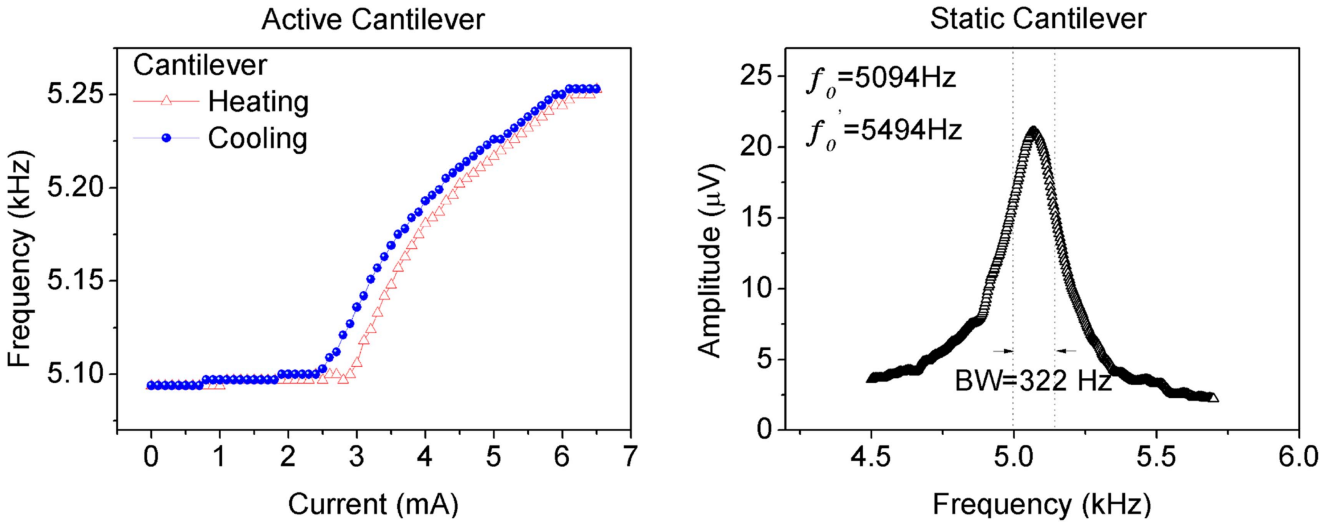

Figure 7. Left: resonant frequency versus actuation current through a full heating and cooling cycle for the active cantilever. Right: resonant frequency signal for the static bridge at room temperature. The measured (f_0) and calculated (f_0') resonant frequencies are shown. The value for f_0' was obtained from equation (2), and it does not take residual thermal stress into account.

During the VO_2 IMT phase transition region, the VO_2 crystal structure changes from its low-temperature monoclinic phase to its high-temperature rutile phase with a contraction in the c-axis [13, 32]. Essentially, the area of the crystal planes parallel to the surface of the substrate is reduced during the phase transition (heating cycle). This generates a compressive stress at the surface of the beam material, which in turn will induce elastic deformation and changes in the geometry of the beam. The deformation will then change the dimensions and the density of the beam, which will further shift the resonant frequency of either the bridge or the cantilever. Thus, the influence of the stress on the resonant frequency is not only due to the induced stress (stress effect) but also caused by geometric variations (geometric effect). However, different beam structures have different responses to the same type of axial stress. For the case of a cantilever (clamped-free structure), the deformation along the longitudinal direction is not constrained and the axial stress is released. This results in a zero net axial stress along the longitudinal direction and a net in-plane stress in the clamped end [33]. For the cantilevers used in this paper, where the width is about 30 times larger than the thickness, the resonant frequency shift is then dominated by the geometric effect and can be described by the following expression [34]:

$$\Delta f/f_r = \{(1 + 2\nu)/(1 - \nu)\}\sigma, \quad (5)$$

where Δf stands for the relative resonant frequency change, ν is the Poisson's ratio, and σ is the applied surface stress. The bridges, on the other hand, have more net axial stress than the cantilevers due to their clamped–clamped structure [25, 30]. The resonant frequency shift is mainly dominated by the stress effect and can be estimated by the following expression [34]:

$$\Delta f/f_r = 0.1475(L/h)^2\sigma, \quad (6)$$

where L and h are the length and thickness of the bridge. Given that the Poisson's of SiO_2 (which makes up for about 90% of the resonator's structure) is 0.2; and the $(L/h)^2$ for the bridges and cantilevers is in the order of 10^4, the frequency shift per stress unit is much larger for the bridges. Furthermore, unlike in the case of a cantilever, the added stress during the phase transition in a clamped–clamped structure is not 'released' in the form of structural bending—unless it reaches the Euler stress limit, which was not the case for the present structures. The resonant frequencies shift for the cantilevers and bridges reported in this manuscript when transitioned across the entire phase transition were about 3.1% and 7.3%, respectively.

3.4. Contributions of the tuning technology

MEMS-based filters have been widely implemented in many applications. Their BW is usually increased by coupling individual resonators into a higher order system. However, most of the devices have BWs and central frequencies that are defined at the time of designing and fabricating the structure, and therefore cannot be adjusted during operation. Thus, tunable filters were proposed for the applications such as channel-selecting [35], WLAN [36], and spectrometers [37], etc. Some tunable MEMS filters focus on the tunability of the central frequency [38, 39], where the tuning operation can be achieved by adjusting the effective length of the resonators that form the filter device. Other devices focus on the tuning of the BW by applying different polarization voltages to the resonators [8]. The present work shows a simple approach to use a new mechanism for simultaneous tuning of the central frequency and BW of a MEMS filter. Although the results are focused on BW tunability, tuning f_o can be achieved by actuation of both resonators. The relative changes in the central frequencies are determined by the hysteresis curves (figures 3-left and 6-left), which are 3.1% for the cantilevers and 7.3% for the bridges. Finally, the crossover of the resonant peaks during actuation in the bridge structure case demonstrates a MEMS filter capable of tuning frequencies

higher or lower than f_o by using an actuation current (I_{act}) of only ~3 mA (as shown in the case of the bridge structure—see figure 4, stages 'a' and 'e').

4. Conclusion

This paper presents VO_2-based tunable MEMS bandpass filters. The resonator structures used in the system were actuated mechanically by piezo-disks driven by the output of a spectrum analyzer; and the mechanical vibrations were monitored optically by using a laser deflection method. The resonant frequency curves of two MEMS structures were measured simultaneously. One of the devices was actuated by current pulses sent through an integrated resistive heater, while the other structure was not actuated. Each current pulse increased the temperature of the mechanical structure, inducing the phase transition of the VO_2 film in the actuated sample. The generated stress during the phase-change of VO_2 induces resonant frequency shifts. Two different resonator structures, cantilevers and bridges, were used to demonstrate fully reversible BW tunability action. The BW was increased 2.39 and 2.62 times the value of a single resonator for the cantilever and bridge system, respectively. The required power for inducing full tuning action in both systems is much larger for the cantilever system (approximately 5.75 mW) than for the bridge system (approximately 0.04 mW). This is due to the much larger sensitivity of the bridge structures to added stress.

Acknowledgments

This work was supported in part by the National Science Foundation under Grant ECCS 1310257 and Grant CMMI 1301243. The authors would like to acknowledge the technical support from the Lurie Nanofabrication facility at University of Michigan for fabricating the devices. The SEM images in figure 1 were taken in the Composite Materials and Structures Center at Michigan State University. The authors are thankful to Professor John Papapolymerou for insightful discussions.

ORCID

Nelson Sepúlveda https://orcid.org/0000-0002-9676-8529

References

[1] Yang Y T, Callegari C, Feng X L, Ekinci K L and Roukes M L 2006 Zeptogram-scale nanomechanical mass sensing *Nano Lett* **6** 583–6
[2] Ma Q, Rossmann T and Guo Z 2008 Temperature sensitivity of silica micro-resonators *J. Phys. D: Appl. Phys.* **41** 245111
[3] Johnson R A, Borner M and Konno M 1971 Mechanical filters-a review of progress *IEEE Trans. Sonics Ultrason.* **18** 155–70
[4] Jung Y, Murugan G S, Brambilla G and Richardson D J 2010 Embedded optical microfiber coil resonator with enhanced high-Q *IEEE Photon. Technol. Lett.* **22** 1638–40
[5] Wang K and Nguyen C T C 1999 High-order medium frequency micromechanical electronic filters *J. Microelectromech. Syst.* **8** 534–56
[6] Greywall D S and Busch P A 2002 Coupled micromechanical drumhead resonators with practical application as electromechanical bandpass filters *J. Micromech. Microeng.* **12** 925–38
[7] Lin L, Howe R T and Pisano A P 1998 Microelectromechanical filters for signal processing *J. Microelectromech. Syst.* **7** 286–94
[8] Pourkamali S and Ayazi F 2005 Electrically coupled mems bandpass filters: II. With coupling element *Sensors Actuators* A **122** 307–16
[9] Desai S, Netravali A and Thompson M 2006 Carbon fibers as a novel material for high-performance microelectromechanical systems (MEMS) *J. Micromech. Microeng.* **16** 1403
[10] Lin Y C, Froemel J, Sharma P, Inoue A, Esashi M and Gessner T 2011 Zr-based metallic glass as a novel mems bonding material *2011 IEEE 24th Int. Conf. on Micro Electro Mechanical Systems (MEMS)* pp 509–12
[11] Heidari A, Yoon Y-J, Lee M I, Khine L, Park M K and Tsai J M L 2013 A novel checker-patterned AIN {MEMS} resonator as gravimetric sensor *Sensors Actuators* A **189** 298–306
[12] Sepúlveda N, Lu J, Aslam D M and Sullivan J P 2008 High-performance polycrystalline diamond micro- and nanoresonators *J. Microelectromech. Syst.* **17** 473–82
[13] Rúa A, Fernández F E and Sepúlveda N 2010 Bending in VO_2 coated microcantilevers suitable for thermally activated actuators *J. Appl. Phys.* **107** 074506
[14] Liu K, Cheng C, Suh J, Tang-Kong R, Fu D, Lee S, Zhou J, Chua L O and Wu J 2014 Powerful multifunctional torsional micromuscles activated by phase transition *Adv. Mater.* **26** 1746–50
[15] Cabrera R, Merced E and Seplveda N 2013 A micro-electro-mechanical memory based on the structural phase transition of VO_2 *Phys. Status Solidi* a **210** 1704–11
[16] Torres D, Wang T, Zhang J, Zhang X, Dooley S, Tan X, Xie H and Sepúlveda N 2016 VO_2-based mems mirrors *J. Microelectromech. Syst.* **25** 780–7
[17] Coy H, Cabrera R, Seplveda N and Fernndez F E 2010 Optoelectronic and all-optical multiple memory states in vanadium dioxide *J. Appl. Phys.* **108** 780–7
[18] Morin F J 1959 Oxides which show a metal-to-insulator transition at the Neel temperature *Phys. Rev. Lett.* **3** 34–6
[19] Barker A S, Verleur H W and Guggenheim H J 1966 Infrared optical properties of vanadium dioxide above and below the transition temperature *Phys. Rev. Lett.* **17** 1286–9
[20] Viswanath B, Ko C H and Ramanathan S 2011 Thermoelastic switching with controlled actuation in VO_2 thin films *Scr. Mater.* **64** 490–3
[21] Cabrera R, Merced E and Sepúlveda N 2014 Performance of electro-thermally driven VO_2-based mems actuators *J. Microelectromech. Syst.* **23** 243–51
[22] Merced E, Cabrera R, Coy H, Fernandez F E and Sepulveda N 2011 Frequency tuning of VO_2-coated buckled microbridges *J. Microelectromech. Syst.* **20** 558–60
[23] Merced E, Torres D, Tan X and Sepúlveda N 2015 An electrothermally actuated VO_2-based mems using self-sensing feedback control *J. Microelectromech. Syst.* **24** 100–7
[24] Merced E, Tan X and Sepúlveda N 2014 Closed-loop tracking of large displacements in electro-thermally actuated VO_2-based mems *J. Microelectromech. Syst.* **23** 1073–83

[25] Merced E, Cabrera R, Dávila N, Fernández F E and Sepúlveda N 2012 A micro-mechanical resonator with programmable frequency capability *Smart Mater. Struct.* **21** 035007
[26] Sepúlveda N, Rúa A, Cabrera R and Fernández F E 2008 Young's modulus of VO_2 thin films as a function of temperature including insulator-to-metal transition regime *J. Appl. Phys Lett.* **92** 5769–76
[27] Pini V, Tamayo J, Gil-Santos E, Ramos D, Kosaka P, Tong H D, Van Rijn C and Calleja M 2011 Shedding light on axial stress effect on resonance frequencies of nanocantilevers *ACS Nano* **5** 4269–75
[28] Cabrera R, Merced E and Sepúlveda N 2014 Performance of electro-thermally driven VO_2-based mems actuators *J. Microelectromech. Syst.* **23** 243–51
[29] Petersan P J and Anlage S M 1998 Measurement of resonant frequency and quality factor of microwave resonators: comparison of methods *J. Appl. Phys.* **84** 3392
[30] Merced E, Cabrera R, Coy H, Fernández F E and Sepúlveda N 2011 Frequency tuning of VO_2-coated buckled microbridges *J. Microelectromech. Syst.* **20** 558–60
[31] Babaei Gavan K, van der Drift E W J M, Venstra W J, Zuiddam M R and van der Zant H S J 2009 Effect of undercut on the resonant behaviour of silicon nitride cantilevers *J. Micromech. Microeng.* **19** 035003
[32] Holsteen A, Kim I S and Lauhon L J 2014 Extraordinary dynamic mechanical response of vanadium dioxide nanowires around the insulator to metal phase transition *Nano Lett.* **14** 1898–902
[33] Lachut M J and Sader J E 2007 Effect of surface stress on the stiffness of cantilever plates *Phys. Rev. Lett.* **99** 206102
[34] Karabalin R B, Villanueva L G, Matheny M H, Sader J E and Roukes M L 2012 Stress-induced variations in the stiffness of micro- and nanocantilever beams *Phys. Rev. Lett.* **108** 236101
[35] Zuo C, Sinha N and Piazza G 2010 Very high frequency channel-select mems filters based on self-coupled piezoelectric aln contour-mode resonators *Sensors Actuators A* **160** 132–40
[36] Kim J M, Lee S, Park J H, Kim J M, Baek C W, Kwon Y and Kim Y K 2006 Mems-based compact dual-band bandpass filters with applications to wireless local area network *J. Micromech. Microeng.* **16** 1135
[37] Lammel G, Schweizer S, Schiesser S and Renaud P 2002 Tunable optical filter of porous silicon as key component for a mems spectrometer *J. Microelectromech. Syst.* **11** 815–28
[38] Entesari K and Rebeiz G M 2005 A differential 4-bit 6.5–10 GHz RF MEMS tunable filter *IEEE Trans. Microw. Theory Tech.* **53** 1103–10
[39] Entesari K and Rebeiz G 2005 A 12–18 GHz three-pole RF MEMS tunable filter *IEEE Trans. Microw. Theory Tech.* **53** 2566–71